DE GRUYTER Nanotechnology Reviews 2021; 10: 1410–1424

Research Article

Tianyu Yu*, Xuandong Mo, Mingjun Chen, and Changfeng Yao

Machine-learning-assisted microstructure–property linkages of carbon nanotube-reinforced aluminum matrix nanocomposites produced by laser powder bed fusion

https://doi.org/10.1515/ntrev-2021-0093
received August 15, 2021; accepted September 13, 2021

Abstract: In this study, the cellular microstructural features in a subgrain size of carbon nanotube (CNT)-reinforced aluminum matrix nanocomposites produced by laser powder bed fusion (LPBF) (a size range between 0.5–1 μm) were quantitatively extracted and calculated from scanning electron microscopy images by applying a cell segmentation method and various image analysis techniques. Over 80 geometric features for each cellular cell were extracted and statistically analyzed using machine learning techniques to explore the structure–property linkages of carbon nanotube reinforced AlSi10Mg nanocomposites. Predictive models for hardness and relative mass density were established using these subgrain cellular microstructural features. Data dimension reduction using principal component analysis was conducted to reduce the feature number to 3. The results showed that even AlSi10Mg nanocomposite specimens produced using different laser parameters exhibited similar Al–Si eutectic microstructures, displaying a large difference in their mechanical properties including hardness and relative mass density due to cellular structure variance. For hardness prediction, the Extra Tress regression models showed a relative error of 2.47% for prediction accuracies. For the relative mass density prediction, the Decision Tress regression models showed a relative error of 1.42% for prediction accuracies. The results demonstrate that the developed models deliver satisfactory performance for hardness and relative mass density prediction of AlSi10Mg nanocomposites. The framework established in this study can be applied to the LPBF process optimization and mechanical properties manipulation of AlSi10Mg-based alloys and other additive manufacturing newly designed alloys or composites.

Keywords: laser powder bed fusion, AlSi10Mg, machine learning, carbon nanotubes, additive manufacturing

1 Introduction

AlSi10Mg as a near eutectic Al–Si alloy is one of the most popular aluminum that has been investigated in laser powder bed fusion (LPBF) [1–5]. AlSi10Mg is a typical casting alloy for thin walls and other complex geometries with superior properties such as high strength, hardness, and good dynamic properties subject to high loads. AlSi10Mg parts can be post-processed such as machining, spark-eroding, welding, shot-peening coating and polishing to meet certain requirements [1–5]. The LPBF of AlSi10Mg can produce small equiaxed grains with a fine pseudoeutectic cellular microstructure due to rapid cooling-induced recrystallization. For a larger AlSi10Mg melt pool, elongated columnar grains were formed [6]. Corse zones can be formed by reheating the base metal to a semi-solid state when the temperature of the alloy is at the mushy zone [7]. The unique near eutectic Al–Si microstructure of the alloy provides its unique properties. The relation between the microstructure and mechanical properties is yet to be determined.

For LBPF fabrication of alloys, a porosity-free highly dense material is usually obtained by tuning prominent

---

*** Corresponding author: Tianyu Yu,** State Key Laboratory of Robotics and System, Harbin Institute of Technology, Harbin 150001, China; School of Mechatronics Engineering, Harbin Institute of Technology, Harbin, 150001, China, e-mail: tianyuyu@hit.edu.cn
Xuandong Mo: School of Mechatronics Engineering, Harbin Institute of Technology, Harbin, 150001, China
Mingjun Chen: State Key Laboratory of Robotics and System, Harbin Institute of Technology, Harbin 150001, China; School of Mechatronics Engineering, Harbin Institute of Technology, Harbin, 150001, China
Changfeng Yao: The Department of Mechanical Engineering and Automation, Northwestern Polytechnical University, Xi'an 710072, China; Key Laboratory of High Performance Manufacturing for Aero Engine, Ministry of Industry and Information Technology, Northwestern Polytechnical University, Xi'an 710072, China

process parameters (*e.g.*, laser power and scan speed), which usually generates a high micro-hardness. Surface roughness is also a consideration and the origin of the vertical roughness in LPBF AlSi10Mg alloy components was investigated [8]. It was found that a contour-first strategy renders a lower vertical roughness compared to a bulk-first strategy. A relatively high level of track energy density should be used on the contours for a smooth surface. Roth *et al.* [9] compared plastic and fracture behavior of cast and LPBF-produced AlSi10Mg samples. About 10% higher yield strength and a 20% higher ultimate tensile strength for the LPBF-produced AlSi10Mg were found compared with cast samples. The LPBF-produced alloy contains much smaller and more ellipsoidal voids with an average radius of 10.7 µm. Laursen *et al.* [10] related porosity of LPBF-produced AlSi10Mg samples to their ductility, yield strength, ultimate tensile strength, and modulus using linear fit, defect susceptibility method and critical local strain method. They found that porosity and ductility are closely related. This study indicates that LPBF-produced macro properties of AlSi10Mg samples such as porosity and roughness could not be solely used to determine their mechanical properties such as yield strength, ultimate tensile strength and hardness. Other microstructure indicators should be explored regarding the microstructure–property linkages. The subgrain size cellular structure was found related to the mechanical behavior of AlSi10Mg. The fine cellular-dendritic solidification structure variance influences the hardness of the specimen and can be tuned using different energy inputs and heat treatment [11]. Liu *et al.* [12] defined two new morphology indices, named dimensional-scale index and the shape index, from scanning electron microscopy images, relating the subgrain size cellular structure of AlSi10Mg to their mechanical properties. They found that the subgrain cell size and cell boundary morphology of the LPBF-fabricated AlSi10Mg strongly alternated their mechanical properties. However, a higher resolution of the subgrain cellular structure representation has not been investigated. Metal matrix composites show superior dynamic behavior and mechanical properties with the addition of reinforcing phase [13,14]. Yu *et al.* [15] found that micro/nano metal matrix composites fabricated using LPBF can provide unique properties over nonreinforced material.

Machine learning as a powerful tool for data-driven modeling has been studied broadly on the process and quality control of smart manufacturing, as well as in performance prediction for additive manufacturing. For example, Zhang *et al.* [16] used extreme gradient boosting and long short-term memory (LSTM) to predict the melt pool temperature in directed energy deposition. It was found that the performance of LSTM is better than extreme gradient boosting where the temperature fluctuations are small. The computational efficiency of LSTM is found much lower than XGBoost. A hybrid Bayesian network has been used to predict the selective laser melting produced 316 L part quality [17]. It was found that after training just four parts from a machine that was not represented in the training data, the predicted mean hardness was within 0.41 predicted standard deviations of the true value, which shows a high prediction accuracy. A significant amount of training data in SLM is required for incorporating more process parameters in the prediction. Wang and Adachi [18] investigated MIPHA and rMIPHA machine learning tools for analyzing steel properties based on 2D/3D microstructural features such as area fraction, circularity, solidity, ferret's diameter/angle, count fraction, volume fraction, surface area, Gauss curvature, ferret's diameter, sphericity, genus, *etc.* The microstructures corresponding to a target stress–strain curve, target tensile strength and total elongation were inversely explored by MIPHA successfully. Fan *et al.* [19] described the complex amorphous structure of metallic glass using a single flexibility-orientated structural quantity, coupled with the pair distribution function of individual atoms through a weighting function. Structure–property correlations are demonstrated including vibrational, diffusional, as well as elastic and plastic relaxation responses. However, high-fidelity data-driven modeling for microstructure–mechanical property linkages of LPBF-produced AlSi10Mg-based composites is yet to be developed.

This study aims to fill the research gap on the subgrain microstructure and mechanical properties linkages of LPBF-produced AlSi10Mg nanocomposites. The effect of laser parameters (laser power and scanning speed) on the produced melt pool morphology and subgrain texture are investigated. The laser parameters influence the porosity formation, as well as the microstructure of the nanocomposites. Machine-learning-based prediction on mechanical properties of AlSi10Mg nanocomposites using microstructural texture features was investigated. This article focuses on developing a characterization and calculation framework for linking microstructural texture variance produced by different laser parameters to the variance of hardness and relative mass density of CNTs/AlSi10Mg nanocomposites. The developed model can be used for material design or process optimization. Principal component analysis was used to assist in detecting the fine microstructure of the nanocomposites and could be modified for other alloys in the future. It shed light on relating the subgrain cellular microstructure of LPBF-produced CNT-reinforced aluminum matrix nanocomposites due to rapid cooling to their mechanical properties.

2 Material and methodology

2.1 Material and the LPBF process

Commercial gas atomized AlSi10Mg powder (a particle size ranges from 25 to 112 µm) and multiwalled carbon nanotubes (MWCNTs with an outer diameter of 3–15 nm, a length of 15–30 µm) without any surface treatment were used as raw materials for carbon nanotube (CNT)-reinforced aluminum matrix nanocomposites (MWCNTs with a mass fraction of 0.5 wt%). An XQM-4 planetary ball milling machine (Changsha Tianchuang Powder Tech Co., China) was used to homogenously deposit MWCNTs on the surfaces of AlSi10Mg powders. The powder mixture was sealed in stainless steel bowls with a steel ball-to-powder ratio of 1:1. The rotation speed was set at 200 rpm with a total milling time of 4 h. After each 15 min of milling, a 5 min rest was set to avoid overheating of the powder mixture. The milled powder was dried in a vacuum chamber for 4 h at a temperature of 80°C and sealed in an aluminum bottle.

The LPBF process was conducted on a commercial SLM system (FS271, Farsoon Tech, Changsha, China) with a 275 mm × 275 mm × 340 mm build volume, consisting of an MFSC-500W ytterbium fiber laser with a maximum power of ~500 W, a spot size of ~90 µm and a continuous wavelength of 1,080 nm. A total of 16 samples fabricated using different scan speeds (1.8–2.4 m/s) and laser powers (350–450 W) were analyzed in this study as shown in Table 1. The detailed material characterization and mechanical testing results of the CNTs/AlSi10Mg nanocomposites were reported elsewhere [20]. Our previous study found that the addition of CNTs can enhance the mechanical properties (*e.g.*, more than 10% yield strength increase) of the nanocomposites compared with AlSi10Mg without the CNT reinforce.

This article aims to build a high fidelity experimental-computational framework for subgrain cellular structure characterization of the CNTs/AlSi10Mg nanocomposites, relating the subgrain microstructure with their mechanical properties in a feature dimension of sub-micrometer to several micrometers.

The relative density of the CNTs/AlSi10Mg nanocomposites is measured using the Archimedes density principle. In addition, the areal density and void identification of micropores were measured using optical images and processed using the algorithm in ImageJ. These two density methods have similar measured values for different samples. Hardness tests were conducted using a Vickers hardness tester (HVS-30, Shanghai Testermachine Co., China) operated at a load of 10 kg and a duration of 5 s. The scanning electron microscopes (SEMs) used in this study are the Zeiss Evo 25 and Phenom ProX (Eindhoven, Netherlands). The SEM images of the subgrain cellular microstructure were taken in 13,000× and 26,000× magnitude. The sample microstructures and melt pool morphology were characterized by optical microscopy (Keyence VH-1000).

Table 1: Laser parameters, measured hardness, and relative density of CNT-reinforced aluminum matrix nanocomposites fabricated by the LPBF process

Sample number	Laser power (W)	Laser scan speed (m/s)	Hardness (HV)	Relative density (%)
1	450	2.4	126.70	96.19
2	450	2.2	123.23	97.94
3	450	2.0	124.29	99.19
4	450	1.8	123.52	98.29
5	416.6	2.4	118.89	95.68
6	416.6	2.2	121.88	96.46
7	416.6	2.0	122.11	98.02
8	416.6	1.8	122.24	97.63
9	383.3	2.4	96.51	93.83
10	383.3	2.2	102.77	95.92
11	383.3	2.0	121.01	98.54
12	383.3	1.8	122.08	98.47
13	350	2.4	99.52	92.02
14	350	2.2	119.97	93.22
15	350	2.0	122.56	96.17
16	350	1.8	119.07	94.71

2.2 Cellular structure image processing scheme

Different melt pool microstructures of about several hundred micrometers size of the as-built CNTs/AlSi10Mg nanocomposites are shown in Figure 1. Figure 1(a) shows the melt pool morphology of the sample top surface with a nearly 45° texture along with the laser scan pattern. Figure 1(b) shows the melt pool morphology of the sample cross-section, showing melt layers formed along the build direction with no apparent micropores or defects. For the top surface melt pool morphology, the melt pool overlaps with each other, making it difficult to quantitively distinguish the melt pool morphology of different laser parameters (*e.g.*, laser power and scanning speed). The nonuniformity of the macro-scale melt pool microstructure may consist of micro-pores as well observed from our previous study, making it further impossible for

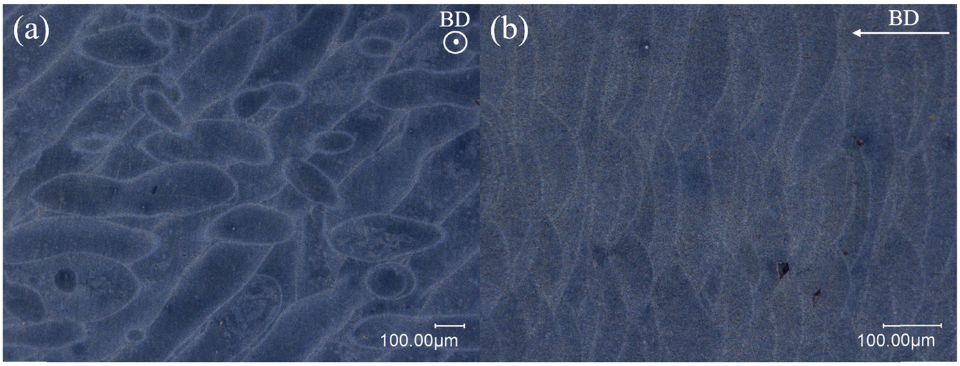

Figure 1: Microscopy of CNTs/AlSi10Mg nanocomposites (the highly dense sample no. 3 with a relative density of 99.3%) showing melt pool morphology: (a) dark field microscopy of the top surface and (b) the cross-section showing melt layers along the build direction with no apparent micropores or defects.

relating the melt pool morphology to their mechanical properties such as hardness and relative density.

To address the issue of correlating the microstructure to mechanical properties, SEM images of the CNTs/AlSi10Mg nanocomposite specimens were processed and characterized to expose their subgrain cellular eutectic structure as shown in Figure 2. The subgrain structure of CNTs/AlSi10Mg nanocomposites exhibits a eutectic and subcellular Al–Si microstructure in a plane perpendicular to the build direction. It can be seen that for sample no.s 1 and 15, laser parameters have a significant effect on the geometry and size of the subgrain cellular microstructure. Most subcells in the fine region have a size range within 0.5–1 µm, while the cell size in the coarse region is about 1–2 µm. α-Al matrix (dark color) is surrounded by a network of Si precipitates (white color) for the fine subgrain region. Discontinuous Si precipitates can be seen in the heat-affected zone (HAZ). The majority phase is fine subgrain instead of the HAZ/coarse subgrain region. Thus, this study is focused on investigating the effect of fine subgrain texture features on the hardness and relative density of CNTs/AlSi10Mg nanocomposites. A total of 96 SEM images of the fine cellular structure were used in this study with six images of each sample. More than 2,000 cells can be detected for each image, so in this study, six images for each sample are assumed adequate to represent the geometry characteristics in the fine cellular zone.

The mechanical properties of the nanocomposites such as surface hardness are related to both bulk

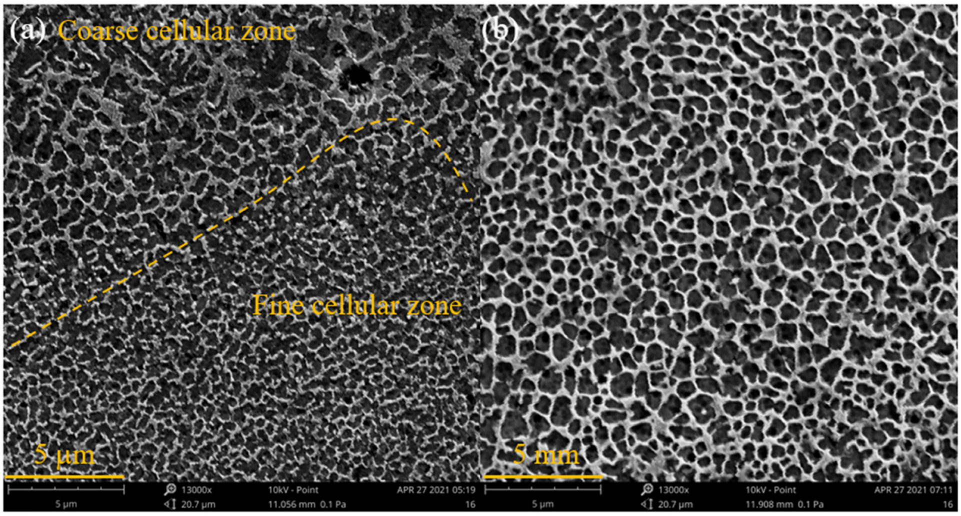

Figure 2: The subgrain textures of CNTs/AlSi10Mg nanocomposites exhibit a eutectic and subcellular Al–Si microstructure in a plane perpendicular to the build direction for (a) sample no. 1 with a laser power of 450 W and a laser scan speed of 2.4 m/s showing fine and coarse cellular microstructure, and (b) sample no. 15 with a laser power of 350 W and a laser scan speed of 2.0 m/s showing a nonuniform fine cell distribution.

properties such as porosity, as well as their unique Al–Si eutectic microstructure. To separate each cell and get their geometric features in an SEM image, cell segmentation software CellProfiler 4.1.3 [21] was used. Several image processing steps were taken to get high-quality cell segmentation features as shown in Figure 3(d):

i) the original SEM image has been black/white-inversed into a gray image to have a better color contrast;

ii) the cell nuclei size is set to a range of 0.15–0.4 µm and then Otsu thresholds [22,23] were used to detect the nuclei of each cellular structure in an SEM image. The Otsu approach is used to calculate and establish optimum threshold separating two classes of pixels (foreground and background) by minimizing the variance within each class by Eq. (1),

$$T_{\text{opt}} = \arg\max\left\{\frac{P(T)[1-P(T)][m_{\text{f}}(T)-m_{\text{b}}(T)]^2}{P(T)\sigma_{\text{f}}^2(T)+[1-P(T)]\sigma_{\text{b}}^2(T)}\right\}, \quad (1)$$

where $P(T)$ is a probability function, $\sigma_{\text{f}}^2(T)$ and $\sigma_{\text{b}}^2(T)$ are variances of foreground and background class, and $m_{\text{f}}(T)$ and $m_{\text{b}}(T)$ are foreground and background class means. This method gives high-quality results when the numbers of pixels in each cell are close to each other (Figure 3(c)).

iii) Based on the nuclei information generated for each cellular structure, the cell geometry and coordination were calculated and are shown in Figure 3(d). The propagation method is used to delineate the boundary between neighboring cells. The minimum cross-entropy is calculated between the foreground

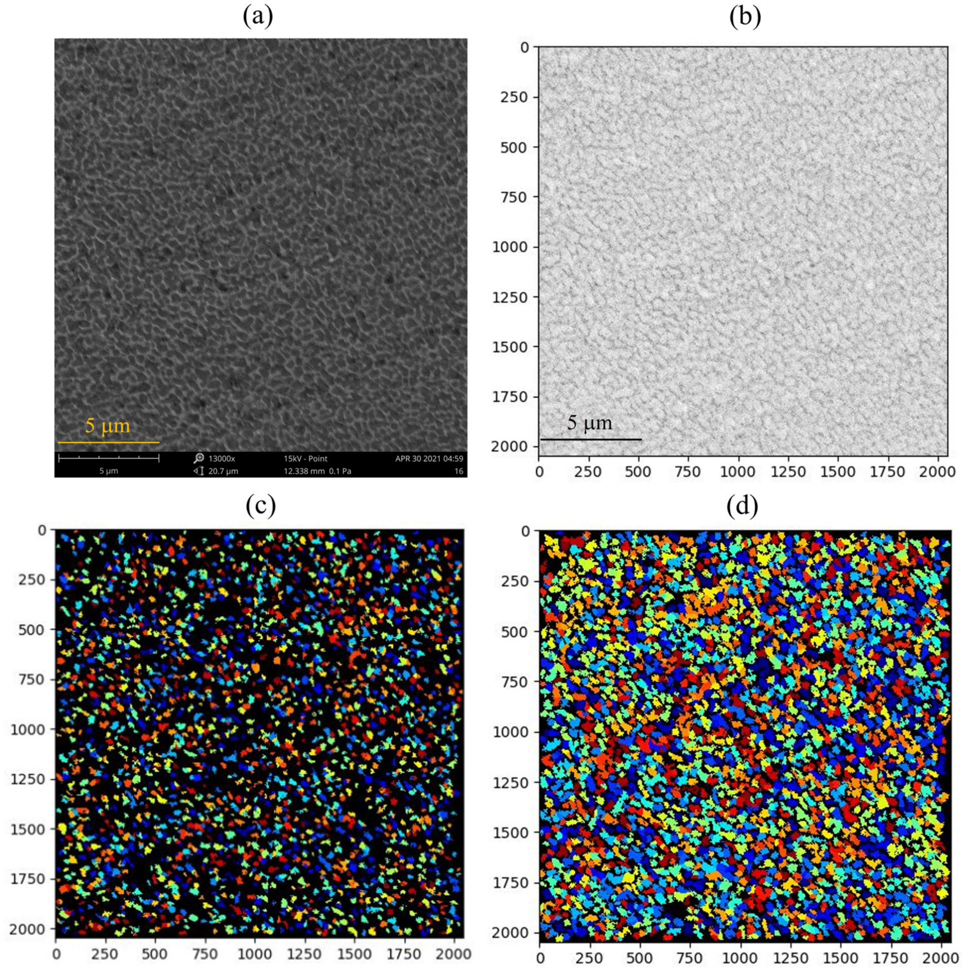

Figure 3: Fine cellular zone cell detection of sample no. 13 of CNTs/AlSi10Mg nanocomposites: (a) the original SEM image of the fine cellular zone in CNTs/AlSi10Mg nanocomposites, (b) the inversed gray image, (c) a cell nuclei map generated from the inversed gray image, and (d) a cell segmentation map showing high fidelity representation of the cell shape and size of the fine cellular zone.

and background distributions (Eq. (2)) and the lowest cross-entropy value is chosen as the final threshold:

$$T_{\mathrm{opt}} = \arg\ \min\left[\sum_{g=0}^{T} gp(g)\log\frac{g}{m_{\mathrm{f}}(T)} + \sum_{g=T+1}^{G} gp(g)\log\frac{g}{m_{\mathrm{b}}(T)}\right], \tag{2}$$

where $\sum_{g\le T} g = \sum_{g\le T} m_{\mathrm{f}}(T)$ and $\sum_{g\ge T} g = \sum_{g\ge T} m_{\mathrm{b}}(T)$.

iv) For example, 2,466 cells were detected in Figure 3(a). The cell geometry characteristics were calculated for each cell. A total of 83 coordinate-independent features were extracted and calculated for each cell. Among all features used in this study, several key features are described as follows:

Perimeter is the length around the boundary of each cell. Eccentricity is the ratio of the distance between the focus points of the ellipse and its major axis length. The value is between 0 and 1 (a circle's eccentricity is 0, while an ellipse with an eccentricity of 1 is a line segment). FormFactor is defined as 4 * π * area/perimeter^2 and the FormFactor of a perfectly circular object is equal to 1. Extent is the proportion of the area in the bounding box that is also in the cell. Solidity is the proportion of the area in the convex hull that is also in the cell. Compactness is the mean squared distance of the cell's pixels from the centroid divided by the area. A filled circle has a compactness of 1. The cells with holes or irregular shapes have a value greater than 1. MeanRadius is the mean distance of any pixel in the object to the closest pixel outside of the cell. Several moments were used to accurately describe the shape and geometry of a cell. For Zernike moments [24], the center of mass for each cell was firstly calculated and a circle is defined. The Zernike moments Z_{nl} for a cell was calculated using

$$Z_{nl} = \frac{n+1}{\pi}\sum_{x}\sum_{y} V_{nl}^{\star}(x,y) f(x,y), \tag{3}$$

where $x^2 + y^2 \le 1,\ \ 0 \le l \le n,\ \ n - l$ is even, and $V_{nl}^{\star}(x,y)$ is the complex conjugate of a nth degree of Zernike polynomial and angular dependence l, and $V_{nl}(x,y)$ is defined as

$$V_{nl}(x,y) = \sum_{m=0}^{(n-l)/2} (-1)^m \frac{(n-m)!}{m!\left[\frac{(n-2m+l)}{2}\right]!\left[\frac{(n-2m-l)}{2}\right]!} \cdot (x^2+y^2)^{(n/2)-m} e^{il\theta}, \tag{4}$$

where $0 \le l \le n,\ \ n - l$ is even, $\theta = \tan^{-1}(y/x)$, and $i = \sqrt{-1}$.

In this study, Zernike polynomials from order 0 to order 9 were calculated and a total of 30 features were calculated. The other moment features are briefly introduced here. Spatial moment features represent a series of weighted averages of shape, size, rotation and location of cells. Central moment features are normalized to the cell's centroid and therefore not influenced by a cell's location within an image. Normalized moment features are further normalized to be scale-invariant and therefore not influenced by a cell's size within an image. Hu moment features are a set of cell moment features that are not altered by the cell's location, size or rotation. Different moments primarily describe the shape of a cell.

The schematic of the proposed cell segmentation and machine-learning assisted microstructure–property linkage framework pipeline for LBPF produced CNTs/AlSi10Mg nanocomposites are shown in Figure 4. The scope of the SEM image processing and cell segmentation is to assess the microstructure cellular distribution of the Si-rich phase and α-Al phase. For the images in which the Si-rich phase is discontinuous, dash dots were connected to form complete cells. The pixels inside a cell can be considered as the α-Al phase and the perimeter can be considered as the Si-rich phase. Then, morphological features for each cellular cell were extracted and calculated, presenting the information of both the Si-rich phase and α-Al phase. As shown in the training phase, 76 randomly selected SEM images were used as the training set. The rest 20 samples were used as the test set. Machine learning algorithms AdaBoost, gradient tree boosting, K-nearest neighbors, decision tree, and extra trees regressors were used to relate the subgrain cellular structure to the mechanical properties of CNTs/AlSi10Mg nanocomposites.

2.3 Machine learning methods

To measure the performance of a machine learning regressor, the root-mean-square error (RMSE) shown in Eq. (5) was used as the performance metric. The RMSE is more sensitive to outliers than the square root of the mean-squared error (MSE) since the effect of each error on RMSE is proportional to the size of the squared error [25]. Relative errors are also calculated:

$$\mathrm{RMSE} = \sqrt{\frac{\sum_{i=1}^{N}(y_{\mathrm{t}} - \hat{y}_{\mathrm{t}})^2}{N}}, \tag{5}$$

$$\mathrm{MSE} = \frac{1}{N}\sum_{i=1}^{N}(y_{\mathrm{t}} - \hat{y}_{\mathrm{t}})^2, \tag{6}$$

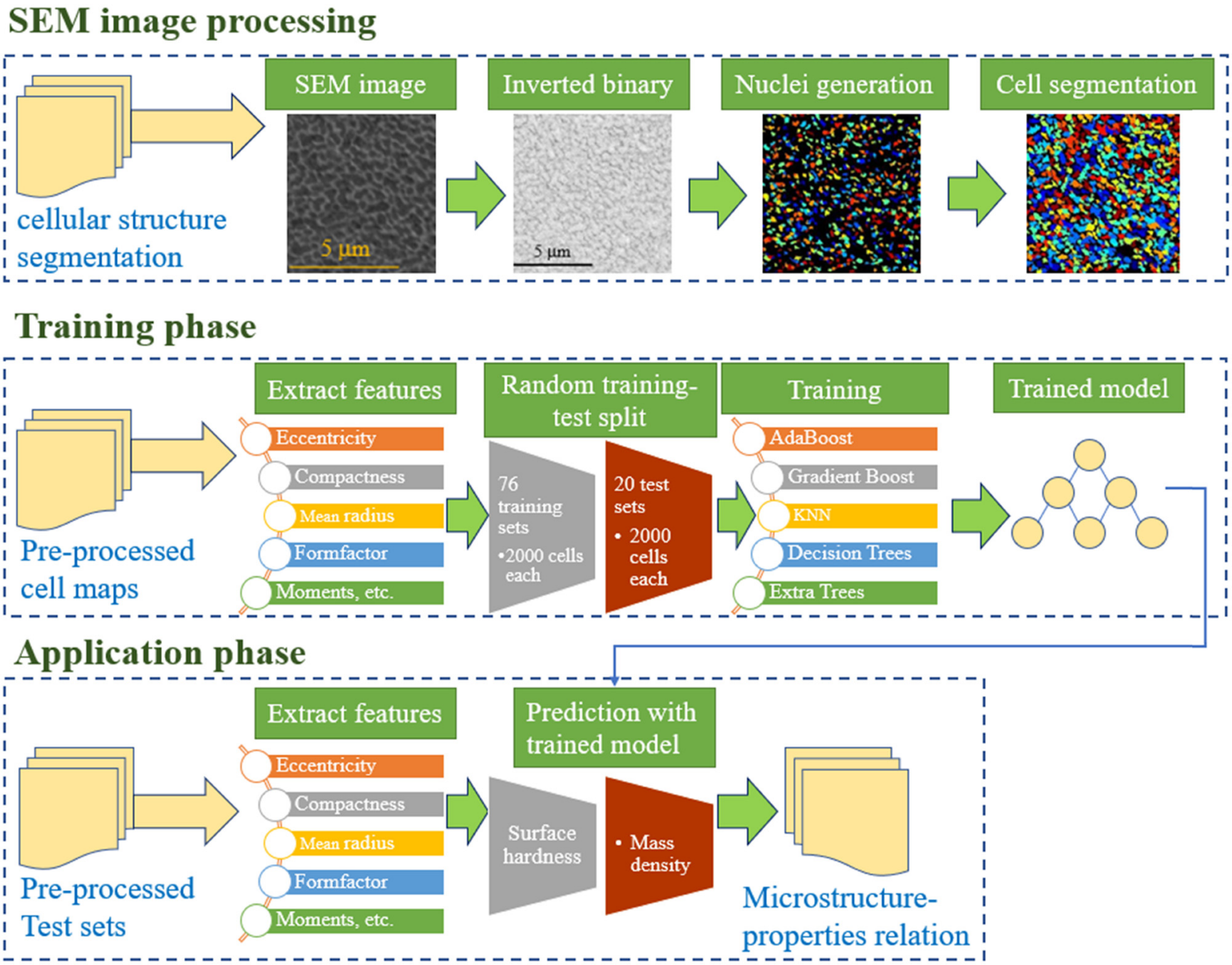

Figure 4: Schematic of the proposed processing framework pipeline for LBPF produced AlSi10Mg nanocomposites microstructure–properties linkages.

where $\hat{y}_t$ is the predicted value of a regression dependent variable y_t and N is the number of data points.

The feature value was mean normalized by using

$$\bar{X} = \frac{X - \text{average}(X)}{\text{stdev}(X)}, \tag{7}$$

where average(X) is the average value of X, and stdev(X) is the standard deviation of X.

Different machine learning regressors were used in this study. AdaBoost is a meta-estimator that fits a regressor on the input dataset and then fits additional copies of the regressor on the same dataset but adjusted the weights of instances according to the error of prediction [26]. Gradient Tree Boosting builds an additive model in a forward stage-wise way [27]. It allows the optimization of arbitrary differentiable loss functions. In each stage, a regression tree is fit on the negative gradient of A given the loss function. KNN is an instance-based method, which uses the input consisting of the k closest training examples in the data set and the output is the property value for the object. The prediction value is the average of the values of k nearest neighbors [28]. Given the input data x and a number of K, the prediction value can be calculated as $\hat{y}_t = (1/K)\sum_{x_i \in N_k(x)} y_i$, where $N_k(x)$ are the K nearest neighbor points to the input x, and y_i represents the output value for each x_i in $N_k(x)$. In KNN regression, the Euclidean or Mahalanobis distance from the query example was calculated to the labeled examples. Then, the labeled examples with increased distance find a heuristically optimal number K of nearest neighbors, based on RMSE through cross-validation. Decision trees are to create a model that predicts the value of a target by learning simple decision rules inferred from the data features. Each tree can be seen as a piecewise constant approximation with each internal node represents a test on an attribute, each branch represents the outcome of the test, and each leaf node represents a class label. It breaks down a dataset into increasingly smaller subsets while an associated decision tree is incrementally developed [29]. Extra Trees, as a tree-based machine learning algorithm, grow a series of unpruned trees with a top-down approach [30]. The Extra Trees uses all training data to build the trees. During the splitting process, a total number of m features are selected randomly as split candidates at each node. The cutting points of each selected feature are also decided randomly. The extreme randomization introduced by feature and cutting point selection will help to further reduce the variance. Three important hyperparameters that need to be tuned are the number of trees, the number of randomly selected features and the minimum number of samples on the leaf nodes. Extra Trees or extremely randomized trees provide another layer of randomness to decision forests algorithms [30]. It implements a meta estimator that fits a number of randomized decision trees on various subsamples of the dataset and averaging algorithm to improve the predictive accuracy and control overfitting. The prediction of this ensemble learning is given as the averaged prediction of the individual classifiers.

A typical form of approximation by Extra Trees is shown as [30]:

$$\hat{y}(x) = \sum_{i_1=0}^{N} \cdots \sum_{i_1=0}^{N} I_{(i_1,\ldots,i_n)}(x) \sum_{X\in(iX_1,\ldots,iX_n)} \lambda^{X}_{(i_1,\ldots,i_n)} \prod_{X_j\in X} x_j, \quad (8)$$

where N is the sample size, $I(i_1,\ldots, i_n)(x)$ is the characteristic function of the hyper-interval, and the real-valued parameters $\lambda^{X}_{(i_1,\ldots,i_n)}$ depend on input x_j and output y_j of the algorithm.

In addition to the original features, principal component analysis [31] is also used in this study for dimensionality reduction by projecting each feature onto several principal components to obtain lower-dimensional features while preserving as much of the data's variation as possible. It is mainly used to explore the internal relationships between large amounts of data. The main principle of the PCA method is to select K (where K is 3 in this study and indicates that data dimensions have been selected) units of orthogonal basis. After the original data is transformed to these three sets of bases, the covariance between each pair of features is set to zero, and the variance between features is as large as possible. In this new space, the information represented by the dimensionality reduction data (three new features) can be used to replace the message of a large amount of data (83 features) in the original space.

3 Results and discussion

3.1 Nanocomposites and cellular structure characterization

After ball milling, CNTs are deposited onto the surface of AlSi10Mg powders. Figure 5 shows the elemental distribution mapping of the ball-milled nanocomposites powder surface with 67.8 wt% aluminum, 25.3 wt% carbon, 6.6 wt% silicon and 0.34 wt% magnesium. The carbon element map reveals a uniform and homogeneous distribution of CNTs on the AlSi10Mg powder surfaces after ball milling, which is a prerequisite for SLM of homogeneous and densification of CNTs/AlSi10Mg nanocomposites.

Three LPBF-produced tensile samples of CNTs/AlSi10Mg nanocomposites are shown in Figure 6(b). A typical yield strength of 380 ± 14 was achieved. A detailed tensile tests analysis is out of the scope of this study and will be reported elsewhere. In order to reveal the melt

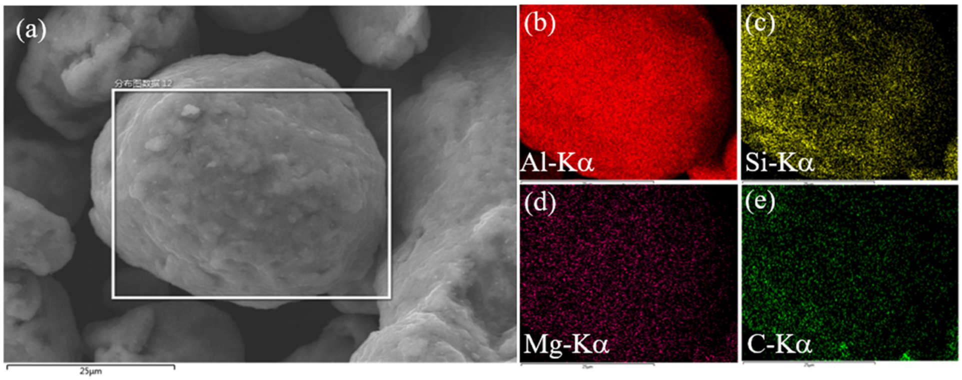

Figure 5: (a) SEM image of the ball-milled CNTs/AlSi10Mg nanocomposite powders with 0.5 wt% CNTs. EDS mapping showing the elemental distribution and concentration of (b) Al, (c) Si, (d) Mg and (e) C on the particle surface.

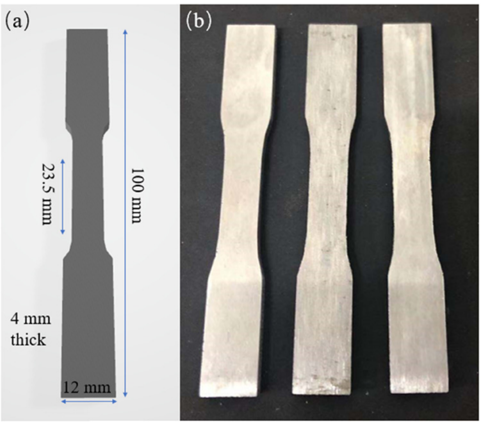

Figure 6: (a) CAD showing tensile bar's dimension; (b) LPBF-produced CNTs/AlSi10Mg nanocomposites tensile samples after machining.

pool morphology, the fractured nanocomposites samples were etched. A Keller solution containing 2.5 mL of HNO_3, 1.5 mL of HCl, 1.0 mL of HF and 95 mL of deionized water was used as an etching agent. Figure 7 shows the crack fronts with respect to the melt pool structure. The melt pool was stretched, showing the structure with a high aspect ratio near the crack front. The CNT phase in the nanocomposites can be also observed. Figure 7(a) and (b) shows the crack propagation path deviations triggered by melt pool boundaries and elongated melt pool structure. Liu *et al.* [12] found that when a crack is confined to the melt pool core regions, the cellular structure provides the main resistance to crack growth. It again suggests the correlation between the subgrain size cellular structure to the mechanical properties of the AlSi10Mg-based composites. Figure 8 shows the tensile specimen fractographs of CNTs/AlSi10Mg nanocomposites; ductile fracture with dimple rupture features was observed. The size of the microdimples is about 0.5–2 µm (shown in Figure 8(c)), which is consistent with the fine cellular size in the core melt pool area.

The unique Al–Si eutectic microstructures of LPBF-produced CNTs/AlSi10Mg nanocomposites exhibited a cellular microstructure as shown in Figure 9(a). Cells in fine and coarse grain/HAZ regions have different shapes and size factors, resulting in a large difference in mechanical properties including hardness and relative mass density of the nanocomposites. The cell segmentation framework was tested on an SEM image of the HAZ coarse cellular zone as shown in Figure 9(b). The HAZ zone, showing a coarse cellular structure, was successfully processed with a high cell segmentation accuracy as shown in Figure 9(d). It can be observed that the cell in the coarse cellular zone has a higher eccentricity value of 0.77 representing elongated cellular grain, a larger cell area value of 16.21 μm^2, a longer perimeter of 2.279 µm and major axis length of 0.628 µm, about 30% higher than those of fine cellular zones. The results showed that the framework proposed in this study is robust and could represent the precise shape and size information for both the fine and HAZ coarse cellular zone of CNTs/AlSi10Mg nanocomposites. The corresponding mean feature values are listed in Table 2. However, the majority phase of the CNTs/AlSi10Mg nanocomposites is the fine cellular structure. Thus, in this study, only fine cellular zones are analyzed and related to their mechanical properties such as hardness and relative mass density.

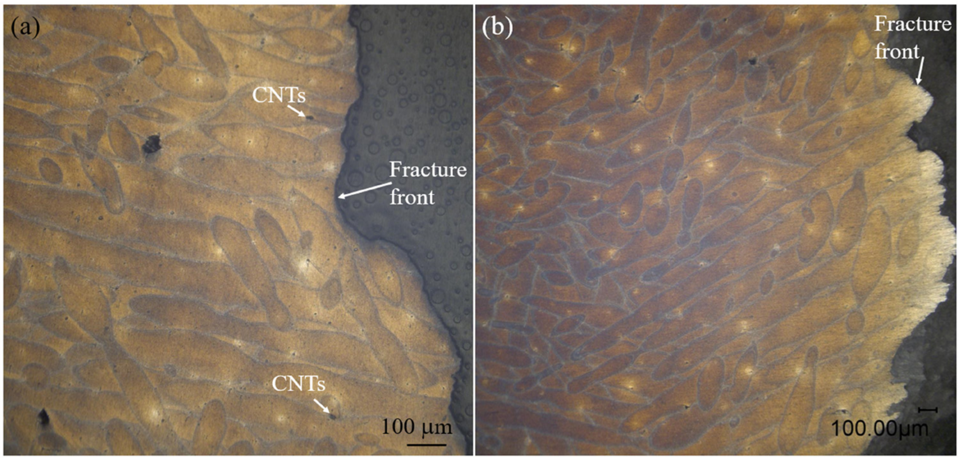

Figure 7: Crack front melt pool morphology of the tensile test specimen showing (a) the crack propagation path deviations triggered by melt pool boundaries and (b) an elongated melt pool structure.

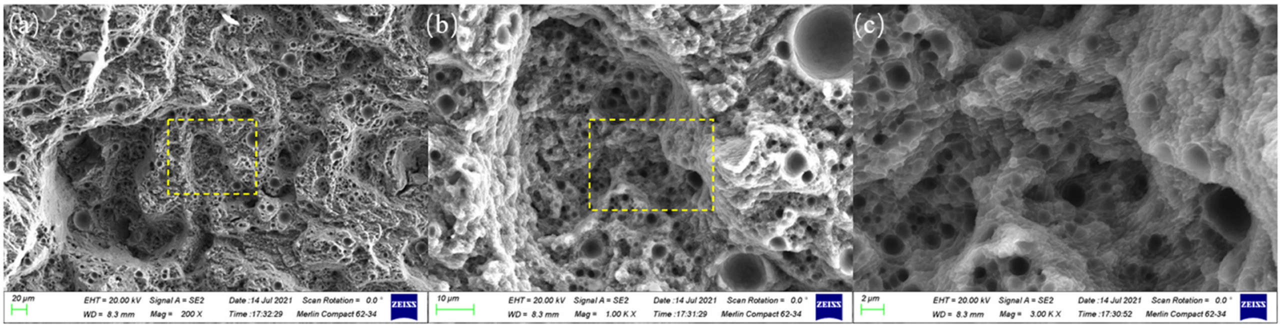

Figure 8: Tensile specimen fractographs of CNTs/AlSi10Mg nanocomposites indicating typical ductile fracture with dimples (a) 200X, (b) 1000X, (c) 3000X.

3.2 Machine learning-based microstructure–property linkages prediction

AdaBoost, GradientBoost, KNN, decision trees, and Extra Trees were used to predict hardness and relative mass density of the CNTs/AlSi10Mg nanocomposites using 83 features generated from the subgrain cellular cell segmentation framework. The features were normalized to avoid any feature bias. Randomly selected 76 SEM images were used as a training set. The rest 20 SEM images were used as a test set for model performance evaluation.

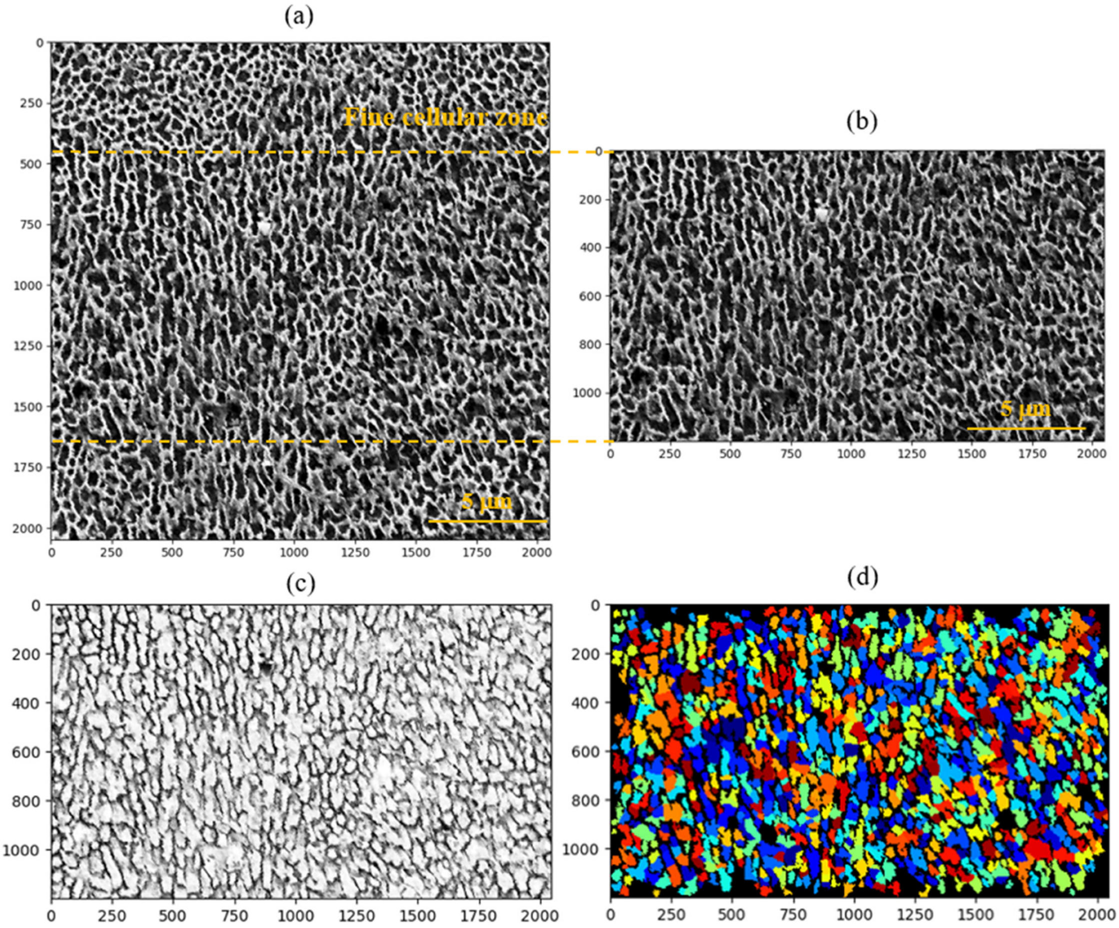

Figure 9: Heat affected zone cellular structure cell detection: (a) subgrain cellular structure of CNTs/AlSi10Mg nanocomposites, (b) the HAZ coarse cellular zone, (c) inversed gray image of the HAZ coarse cellular zone and (d) the HAZ coarse cellular zone cell segmentation shows high fidelity representation of the cell shape and size.

Table 2: Mean feature values of cells in HAZ and fine cellular zones

Feature	HAZ zone	Fine cellular zone
Area (μm^2)	16.21	12.54
Perimeter (μm)	2.279	1.875
Major axis length (μm)	0.628	0.521
Minor axis length (μm)	0.355	0.327
Eccentricity	0.77	0.72
Form factor	0.42	0.48
Extent	0.53	0.56
Solidity	0.78	0.82
Compactness	2.72	2.34
Euler number	0.99	0.98

Feature importance was calculated using AdaBoost, decision tree and Extra Trees regressor (Figure 10). It can be seen that the five most important features for AdaBoost to determine the hardness of the CNTs/AlSi10Mg nanocomposites are Zernike moment 2_0 (9.92%), perimeter (8.48%), eccentricity (7.52%), compactness (6.77%), and maximum radius (5.14%). For decision tree regressor, the five most important features are eccentricity (33.52%), mean radius (28.19%), extent (17.74%), orientation (8.86%) and formfactor (6.34%). For Extra Trees, the 5 most important features are Zernike moment 5_3 (9.92%), Zernike moment 2_0 (9.92%), eccentricity (9.03%), formfactor (7.18%), and compactness (6.42%), showing the aspect ratio of the subgrain cell shape and size are crucial to the mechanical properties of the CNTs/AlSi10Mg nanocomposites. In all cases, eccentricity is one of the key features for the prediction of mechanical properties.

The model predictive results were plotted against the original data for hardness and relative mass density of CNTs/AlSi10Mg nanocomposites. It can be seen from Figure 11 that high accuracy was achieved for the predicted hardness values. Table 3 lists the performance metrics for different machine learning algorithms. AdaBoost has the best prediction performance with an RMSE of 5.936 HV, an MSE of 35.239 HV^2 and a RE of 2.47%. Extra Trees have the prediction performance of the largest error with an RMSE of 8.402 HV, an MSE of 70.596 HV^2 and a RE of 5.30%. Even the worst machine learning algorithm in this study can render a RE of 5.30%, showing the strong correlation between subgrain cellular structure and the mechanical properties of CNTs/AlSi10Mg nanocomposites. For relative mass density prediction, the decision tree method has the highest prediction accuracy with an RMSE of 2.36%, an MSE of 0.0558% and a RE of 1.59%. It provides better predictive performance over the other base learners (Table 4).

Figure 12 shows the SEM image and cell segmentation maps for low hardness (99.52 HV) and high hardness (124.29 HV) samples with good machine learning model prediction accuracy. The key feature values for low hardness samples are eccentricity, 0.75; mean radius, 3.69 pixels; compactness, 7.18; perimeter, 3.47 μm; extent, 0.46; and zernike_2_0–0.15. The key feature values for high hardness sample are eccentricity, 0.76; mean radius, 3.56; compactness, 5.47; perimeter, 2.65 μm; extent, 0.46; and zernike_2_0–0.16. With a similar mean radius value, the smaller compactness and perimeter can render a higher surface hardness. These results show that the proposed model can predict mechanical properties very well with subgrain cellular features as input. The cause for outliers such as sample no. 14 in Figure 11 may be due to the limited SEM images used in this study but it again suggests the model developed in this study can produce

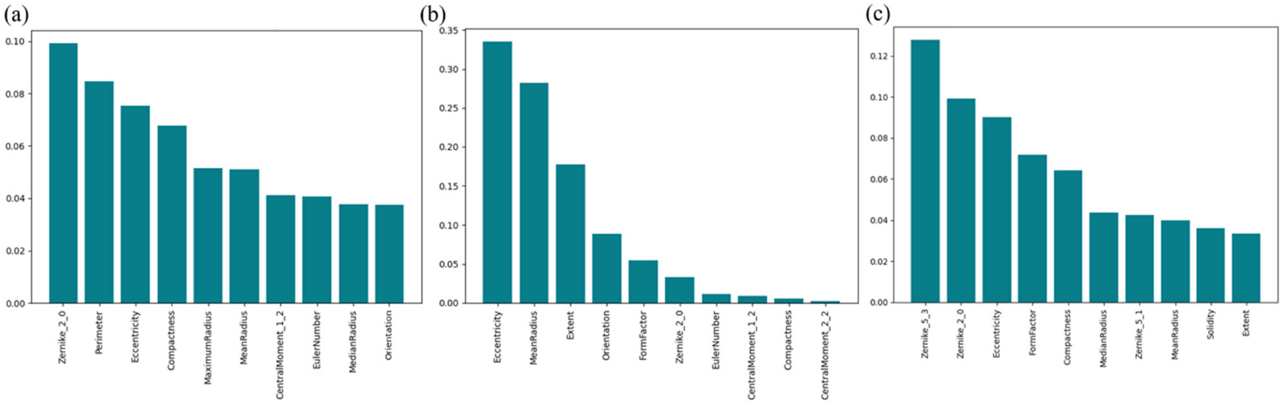

Figure 10: Feature importance rank to predict hardness of CNTs/AlSi10Mg nanocomposites for different ML methods: (a) AdaBoost, (b) decision tree, and (c) Extra Trees.

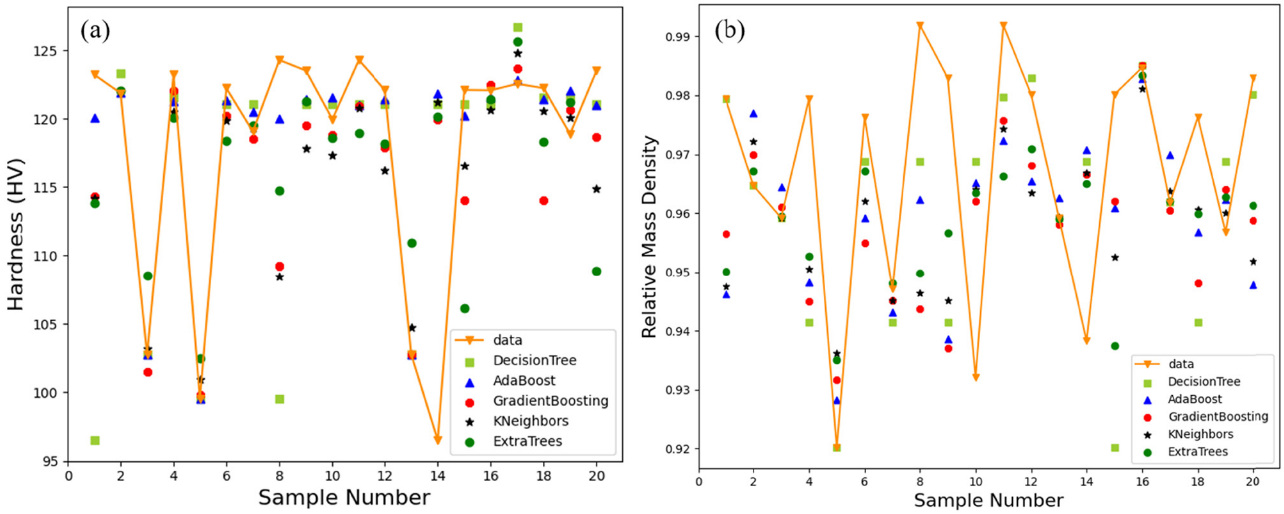

Figure 11: (a) Surface hardness and (b) relative mass density prediction of CNTs/AlSi10Mg nanocomposites using different ML methods with subgrain cellular structure features as input.

Table 3: Surface hardness prediction performance using different ML methods

ML method	RMSE (HV)	MSE (HV^2)	RE (%)
AdaBoost	**5.936**	**35.239**	**2.47**
GradientBoost	7.131	50.855	3.86
KNN	7.629	58.213	4.37
Decision trees	8.535	72.853	4.04
Extra Trees	8.402	70.596	5.30

Bold values stand for the best performance in the prediction.

Table 4: Relative mass density prediction performance using different ML methods

ML method	RMSE (%)	MSE (%)	RE (%)
AdaBoost	2.26	0.0515	1.95
GradientBoost	2.30	0.0530	1.85
KNN	2.27	0.0514	1.86
Decision trees	**2.36**	**0.0558**	**1.59**
Extra Trees	2.17	0.0469	1.72

Bold values stand for the best performance in the prediction.

relatively accurate results with even limited data for the training set.

3.3 Principal component analysis of prediction of microstructure–property linkages

PCA normalizes the high dimension feature dataset (83 features in this study) with correlated variables and converts it into a set of linearly uncorrelated vectors that can describe the variances of the features. Three principal components PC_1, PC_2 and PC_3 are used in this study for reducing the dimensionality of the feature datasets, evaluating the primary variances of the observations.

The PCA model predictive results are plotted against the original data for hardness and relative mass density of CNTs/AlSi10Mg nanocomposites. The hardness prediction performance after PCA decomposition is shown in Figure 13 and Table 5. The best performance machine learning algorithm compared with before PCA decomposition changes to Extra Tress from AdaBoost. The original RMSE of 5.936 HV, an MSE of 35.239 HV^2 and a RE of 2.47% were changed to 6.313 HV, 39.858 HV^2 and 3.61%, respectively. The predictive accuracy becomes a little worse but with PCA dimensional reduction, the number of features became much less, making it easier for SEM image data registration, especially for a large amount of data handling.

The relative mass density prediction performance after PCA decomposition is shown in Figure 14 and Table 6. The best performance algorithm compared to before PCA decomposition changes to AdaBoost from decision trees. The original RMSE of 2.36%, an MSE of 0.0558% and a RE of 1.59% were improved to 1.71, 0.0294 and 1.42%, respectively. The predictive accuracy

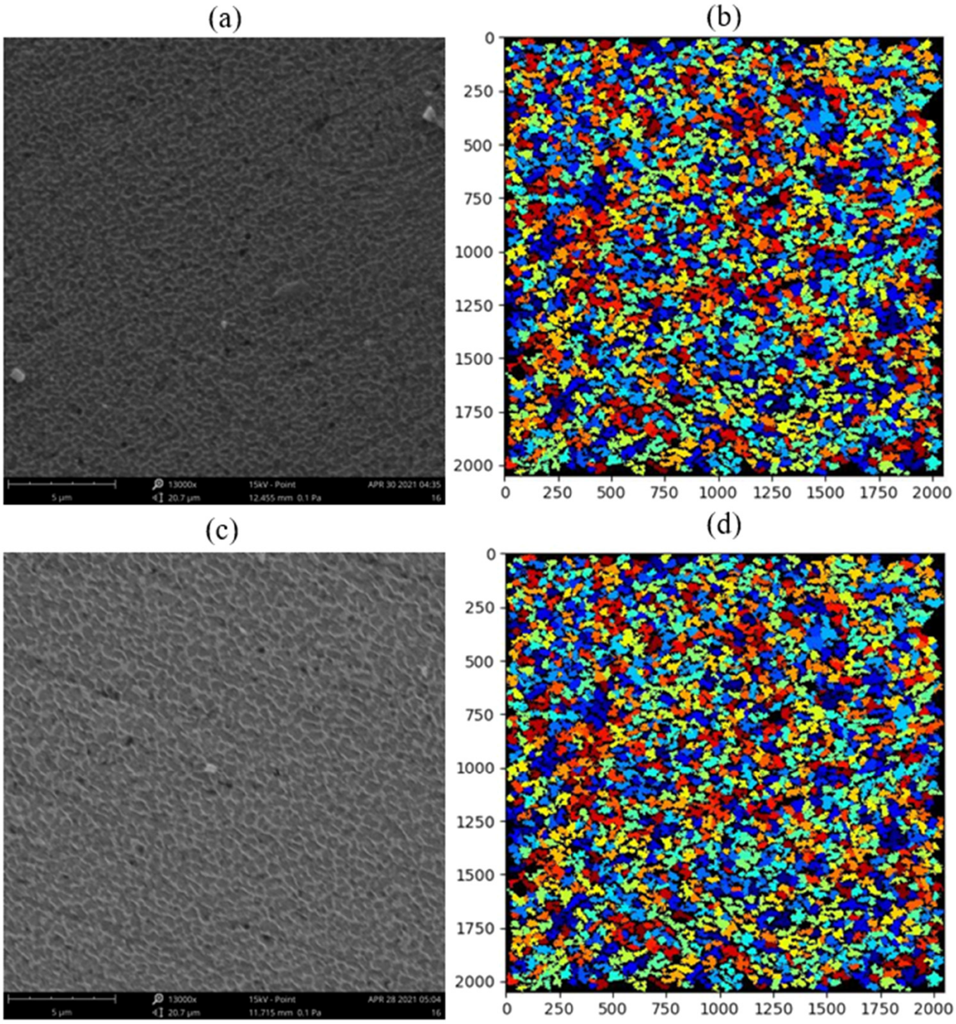

Figure 12: Low hardness (99.52 HV) and high hardness (124.29 HV) samples with good prediction accuracy: (a) and (b) low hardness sample (sample no. 5 in Figure 11) SEM image and cell segmentation map; (c) and (d) high hardness sample (sample no. 8 in Figure 11) SEM image and cell segmentation map.

for relative mass density becomes better with PCA dimensional reduction, demonstrating the PCA decomposition contains the main shape and geometry information of the major features.

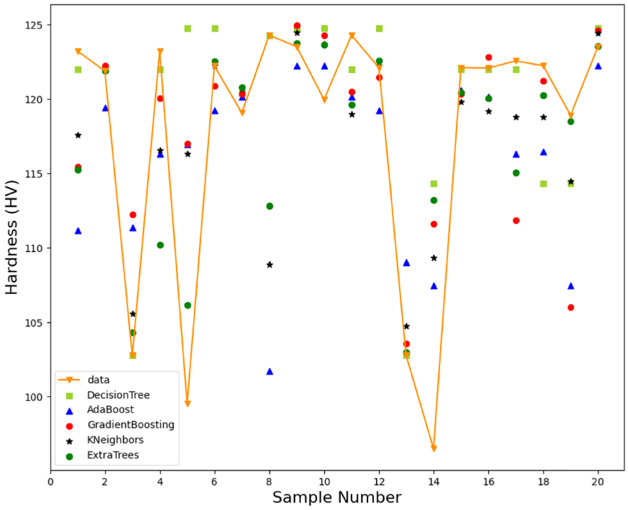

Figure 13: Surface hardness prediction of CNTs/AlSi10Mg nanocomposites using different ML methods with PCA decomposition reduced features.

Table 5: Surface hardness prediction performance using different ML methods with PCA decomposition features

ML method	RMSE (HV)	MSE (HV^2)	RE (%)
AdaBoost	8.659	74.986	5.71
GradientBoost	7.587	57.556	4.77
KNN	6.627	43.918	4.09
Decision trees	7.382	54.488	**3.51**
Extra Trees	**6.313**	**39.858**	3.61

Bold values stand for the best performance in the prediction.

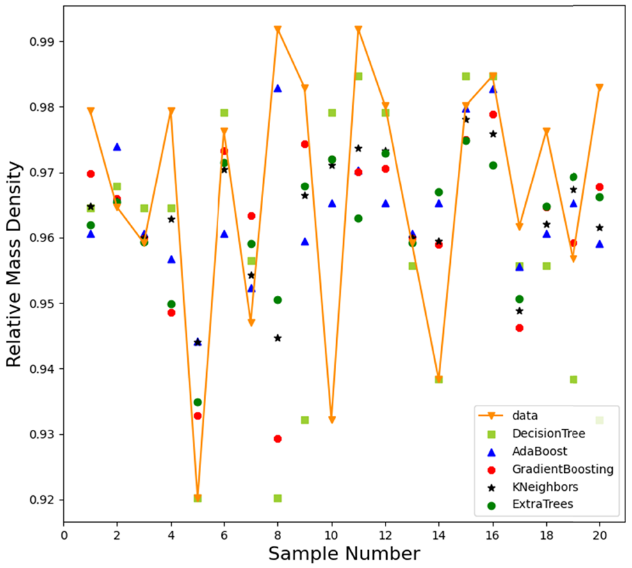

Figure 14: Relative mass density prediction of CNTs/AlSi10Mg nanocomposites using different ML methods with PCA decomposition reduced features.

Table 6: Relative mass density prediction performance using different ML methods with PCA decomposition features

ML method	RMSE (%)	MSE (%)	RE (%)
AdaBoost	**1.71**	**0.0294**	**1.42**
GradientBoost	2.09	0.0437	1.51
KNN	1.87	0.0350	1.50
Decision trees	2.64	0.0699	1.71
Extra Trees	1.96	0.0385	1.61

Bold values stand for the best performance in the prediction.

4 Conclusions

CNT-reinforced aluminum matrix nanocomposites were successfully fabricated with different laser powers and scanning speeds. The unique Al–Si eutectic cellular microstructures and densification behavior during laser melting were examined.

A cellular structure segmentation framework was proposed to extract the cell geometric features. Machine-learning-assisted microstructure–property linkages were explored, successfully predicting the hardness and relative mass density with high accuracy. This study is one of the first works that is addressing microstructure–property linkages of LPBF-produced AlSi10Mg-based composites. The major findings of this study are summarized as follows:

1) The melt pool structure of the fractured tensile samples was stretched, showing the microstructure with a high aspect ratio near the crack front. The CNT phase in the nanocomposites was observed. The crack propagation path deviations triggered by melt pool boundaries and the cellular structure provide the main resistance to crack growth. The correlation between the subgrain size cellular structure to the mechanical properties of the nanocomposites was found to be prominent. The dimension, size and shape of a eutectic subcell are different for various laser parameters. The cell in the coarse cellular zone has a higher eccentricity value, a larger cell area value and a longer perimeter.
2) Cellular zone cell segmentation was successfully achieved by inverting the image, cell nuclei search and cell generation. Cells in both the fine cellular zone and coarse cellular zone of CNTs/AlSi10Mg nanocomposites were successfully represented and 83 geometric features were extracted for each individual cell. Zernike moment 2_0, perimeter, eccentricity and mean radius were found to be the key microstructural features that affected the mechanical properties of a nanocomposites specimen.
3) Machine learning algorithms such as AdaBoost, gradient tree boosting, *K*-nearest neighbors, decision tree, and Extra Trees regressors were used to successfully predict the hardness and relative mass density of CNTs/AlSi10Mg nanocomposites, correlating the mechanical properties with geometric features of cellular zone cells. The prediction relative error is as low as 3.61 and 1.42% for hardness and relative mass density using principal component analysis, respectively.

Funding information: This work was supported by Project 52005133 of National Natural Science Foundation of China, Self-Planned Task (No. SKLRS202002C) of State Key Laboratory of Robotics and System (HIT), Research Fund of Key Laboratory of High Performance Manufacturing for Aero Engine (Northwestern Polytechnical University), Ministry of Industry and Information Technology (Grant No.HPM-2020-08), and the Fundamental Research Funds for the Central Universities (No. AUGA5710050320).

Author contributions: All authors have accepted responsibility for the entire content of this manuscript and approved its submission.

Conflict of interest: The authors state no conflict of interest.

Data availability statement: The datasets generated during and/or analyzed during the current study are available from the corresponding author on reasonable request.

References

[1] Yu T, Hyer H, Sohn Y, Bai Y, Wu D. Structure-property relationship in high strength and lightweight AlSi10Mg microlattices fabricated by selective laser melting. Mater Des. 2019;182:108062.

[2] Kempen K, Thijs L, Van Humbeeck J, Kruth J-P. Mechanical properties of AlSi10Mg produced by selective laser melting. Phys Proc. 2012;39:439–46.

[3] Read N, Wang W, Essa K, Attallah MM. Selective laser melting of AlSi10Mg alloy: Process optimisation and mechanical properties development. Mater Des (1980–2015). 2015;65:417–24.

[4] Wu J, Wang X, Wang W, Attallah M, Loretto M. Microstructure and strength of selectively laser melted AlSi10Mg. Acta Mater. 2016;117:311–20.

[5] Girelli L, Tocci M, Gelfi M, Pola A. Study of heat treatment parameters for additively manufactured AlSi10Mg in comparison with corresponding cast alloy. Mater Sci Eng: A. 2019;739:317–28.

[6] Thijs L, Kempen K, Kruth J-P, Van Humbeeck J. Fine-structured aluminium products with controllable texture by selective laser melting of pre-alloyed AlSi10Mg powder. Acta Mater. 2013;61(5):1809–19.

[7] Liu X, Zhao C, Zhou X, Shen Z, Liu W. Microstructure of selective laser melted AlSi10Mg alloy. Mater Des. 2019;168:107677.

[8] Poncelet O, Marteleur M, van der Rest C, Rigo O, Adrien J, Dancette S, et al. Critical assessment of the impact of process parameters on vertical roughness and hardness of thin walls of AlSi10Mg processed by laser powder bed fusion. Addit Manuf. 2021;38:101801.

[9] Roth CC, Tancogne-Dejean T, Mohr D. Plasticity and fracture of cast and SLM AlSi10Mg: high-throughput testing and modeling. Addit Manuf. 2021;43:101998.

[10] Laursen CM, DeJong SA, Dickens SM, Exil AN, Susan DF, Carroll JD. Relationship between ductility and the porosity of additively manufactured AlSi10Mg. Mater Sci Eng: A. 2020;795:139922.

[11] Fousová M, Dvorský D, Michalcová A, Vojtěch D. Changes in the microstructure and mechanical properties of additively manufactured AlSi10Mg alloy after exposure to elevated temperatures. Mater Charact. 2018;137:119–26.

[12] Liu Q, Wu H, Paul MJ, He P, Peng Z, Gludovatz B, et al. Machine-learning assisted laser powder bed fusion process optimization for AlSi10Mg: new microstructure description indices and fracture mechanisms. Acta Mater. 2020;201:316–28.

[13] Fan J, Wang C. Dynamic compressive response of a developed polymer composite at different strain rates. Compos Part B: Eng. 2018;152:96–101.

[14] Liu Y, Van der Meer F, Sluys LJ, Fan J. A numerical homogenization scheme used for derivation of a homogenized viscoelastic-viscoplastic model for the transverse response of fiber-reinforced polymer composites. Compos Struct. 2020;252:112690.

[15] Yu T, Guo W, Wang X, Liu J, Wang Y, Chen M. Surface hydrophobicity and oleophilicity of hierarchical metal structures fabricated using ink-based selective laser melting of micro/nanoparticles. Nanotechnol Rev. 2020;9(1):626.

[16] Zhang Z, Liu Z, Wu D. Prediction of melt pool temperature in directed energy deposition using machine learning. Addit Manuf. 2021;37:101692.

[17] Hertlein N, Deshpande S, Venugopal V, Kumar M, Anand S. Prediction of selective laser melting part quality using hybrid Bayesian network. Addit Manuf. 2020;32:101089.

[18] Wang Z-L, Adachi Y. Property prediction and properties-to-microstructure inverse analysis of steels by a machine-learning approach. Mater Sci Eng: A. 2019;744:661–70.

[19] Fan Z, Ding J, Ma E. Machine learning bridges local static structure with multiple properties in metallic glasses. Mater Today. 2020;40:48–62.

[20] Yu T, Liu J, He Y, Tian J, Chen M, Wang Y. Microstructure and wear characterization of carbon nanotubes (CNTs) reinforced aluminum matrix nanocomposites manufactured using selective laser melting. Wear. 2020;203581.

[21] Carpenter AE, Jones TR, Lamprecht MR, Clarke C, Kang IH, Friman O, et al. CellProfiler: image analysis software for identifying and quantifying cell phenotypes. Genome Biol. 2006;7(10):1–11.

[22] Otsu N. A threshold selection method from gray-level histograms. IEEE Trans Syst, Man, Cybern. 1979;9(1):62–6.

[23] Sezgin M, Sankur B. Survey over image thresholding techniques and quantitative performance evaluation. J Electron Imaging. 2004;13(1):146–65.

[24] Boland MV, Markey MK, Murphy RF. Automated recognition of patterns characteristic of subcellular structures in fluorescence microscopy images. Cytometry: J Int Soc Anal Cytol. 1998;33(3):366–75.

[25] Shi J, Yu T, Goebel K, Wu D. Remaining useful life prediction of bearings using ensemble learning: the impact of diversity in base learners and features. J Comput Inf Sci Eng. 2021;21(2):021004.

[26] Freund Y, Schapire RE. A decision-theoretic generalization of on-line learning and an application to boosting. J Comput Syst Sci. 1997;55(1):119–39.

[27] Friedman JH. Stochastic gradient boosting. Comput Stat Data Anal. 2002;38(4):367–78.

[28] Burba F, Ferraty F, Vieu P. k-Nearest neighbour method in functional nonparametric regression. J Nonparametr Stat. 2009;21(4):453–69.

[29] Safavian SR, Landgrebe D. A survey of decision tree classifier methodology. IEEE Trans Syst, Man, Cybern. 1991;21(3):660–74.

[30] Geurts P, Ernst D, Wehenkel L. Extremely randomized trees. Mach Learn. 2006;63(1):3–42.

[31] Wold S, Esbensen K, Geladi P. Principal component analysis. Chemomet Intell Lab Syst. 1987;2(1–3):37–52.